ACS APPLIED MATERIALS & INTERFACES

www.acsami.org Research Article

Modulation of Structural, Electronic, and Optical Properties of Titanium Nitride Thin Films by Regulated In Situ Oxidation

Manosi Roy, Kaushik Sarkar, Jacob Som, Mark A. Pfeifer, Valentin Craciun, J. David Schall, Shyam Aravamudhan, Frank W. Wise, and Dhananjay Kumar*

Cite This: *ACS Appl. Mater. Interfaces* 2023, 15, 4733−4742 Read Online

ABSTRACT: Epitaxial titanium nitride (TiN) and titanium oxynitride (TiON) thin films have been grown on sapphire substrates using a pulsed laser deposition (PLD) method in high-vacuum conditions (base pressure $<3 \times 10^{-6}$ T). This vacuum contains enough residual oxygen to allow a time-independent gas phase oxidation of the ablated species as well as a time-dependent regulated surface oxidation of TiN to TiON films. The time-dependent surface oxidation is controlled by means of film deposition time that, in turn, is controlled by changing the number of laser pulses impinging on the polycrystalline TiN target at a constant repetition rate. By changing the number of laser pulses from 150 to 5000, unoxidized (or negligibly oxidized) and oxidized TiN films have been obtained with the thickness in the range of four unit cells to 70 unit cells of TiN/TiON. X-ray photoelectron spectroscopy (XPS) investigations reveal higher oxygen content in TiON films prepared with a larger number of laser pulses. The oxidation of TiN films is achieved by precisely controlling the time of deposition, which affects the surface diffusion of oxygen to the TiN film lattice. The lattice constants of the TiON films obtained by x-ray diffraction (XRD) increase with the oxygen content in the film, as predicted by molecular dynamics (MD) simulations. The lattice constant increase is explained based on a larger electrostatic repulsive force due to unbalanced local charges in the vicinity of Ti vacancies and substitutional O. The bandgap of TiN and TiON films, measured using UV−visible spectroscopy, has an asymmetric V-shaped variation as a function of the number of pulses. The bandgap variation following the lower number of laser pulses (150−750) of the V-shaped curve is explained using the quantum confinement effect, while the bandgap variation following the higher number of laser pulses (1000−5000) is associated with the modification in the band structure due to hybridization of O_{2p} and N_{2p} energy levels.

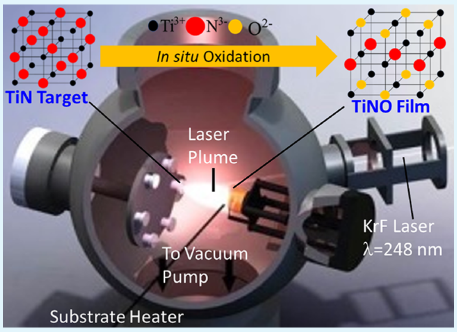

KEYWORDS: *thin films, pulsed laser deposition, controlled oxidation, bandgap energy, oxynitrides, transition metal nitrides*

1. INTRODUCTION

Providing clean and renewable energy is among the most critical challenges of the 21st century.[1−3] Overcoming the energy challenge requires new conversion technologies that can meet the growing global energy demand, which is projected to rise to 24−26 TW in 2040.[3] The conversion technologies should be able to mitigate the rapidly increasing carbon dioxide emissions. The present research aims to design a titanium metal-based oxynitride (TiNO) homolog series capable of supporting energy conversion reactions and to understand materials' fundamental physical and chemical properties across different length scales. The transition metal oxynitrides (TMONs) such as TiNO[4−13] are preferred over relatively more familiar transition metal oxides (TMOs) in the fields of solar water-splitting and photovoltaic solar cells.[14−20] The preference arises as TMONs are usually optically more active in the visible light range in comparison to TMOs.[9] This difference in the physical and chemical properties of TMONs and TMOs arises from the less electronegative and more polarizable characteristics of nitrogen than that of oxygen.[11,18,19] Low bandgap, moderate electrical conductivity, and good stability in low pH media are some of the added advantages TMONs can offer over TMOs.[11,12]

The general formula of the TiNO homolog series, which usually contains Ti vacancies, as it will be shown later, is expressed as $\mathrm{Ti}^{3+}_{(1-x/3)}\mathrm{Ti(vac)}^{3+}_{x/3}\mathrm{N}^{3-}_{(1-x)}\mathrm{O}^{2-}_{x}$. The series exists in the whole range of $0 \leq x \leq 1$.[21] In this formula, Ti^{3+} (vac) is the number of Ti^{3+} vacancies in each formula unit. This molecular formula takes into account the substitution of trivalent N anions by bivalent O anions in an ionic TiN lattice and the maintenance of charge neutrality in the lattice. The formula is also built on the assumption that the valences of Ti,

Received: October 20, 2022
Accepted: December 30, 2022
Published: January 10, 2023

https://doi.org/10.1021/acsami.2c18926

N, and O are maintained at +3, −3, and − 2, respectively. The terminal compounds (TiN with $x = 0$ and TiO with $x = 1$) as well as all the intermediate compounds with x between 0 and 1 have a rock-salt structure (Figure 1), but they possess wide-ranging physicochemical properties.[22] One of the terminal compounds of the family, TiN ($x = 0$), has been known for its well-established properties for decades.[23−28] A controlled variation of oxygen in TiNO can be used in the fabrication of multijunction solar cells,[29] electrocatalysts,[23] photoelectrocatalysts,[30−32] photodetectors,[33,34] and plasmonic[35,36] and metamaterial devices.[37−39] Our success in producing semiconducting TiNO with room-temperature conductivity (~158−6493 Ω^{-1} cm^{-1}) significantly higher than that of carbon (~1 Ω^{-1} cm^{-1}) may open up the door for the development of carbon-free support materials as an electrocatalyst/photoelectrocatalyst in water-splitting research.

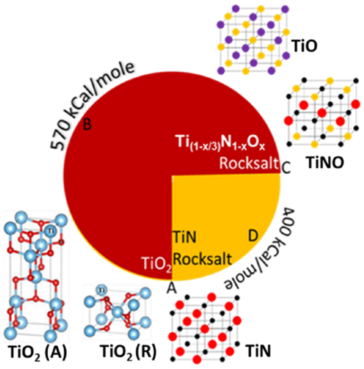

Figure 1. Schematic representation of oxidation and nitridation energetics and crystal structures of rutile and anatase TiO_2, TiN, $TiN_{0.5}O_{0.5}$, and TiO; the respective ionic radii are Ti^{3+} (blue circle) = 0.081 nm, Ti^{2+} (purple circle) 0.125 nm, N^{3-} (red circle) = 0.132 nm, and O^{2-} (yellow circle) = 0.100 nm.[20] Points A and C represent the starting materials: anatase (A), rutile (R) TiO_2, or rock-salt (RS) TiN and product materials, RS TiO or RS TiNO, formed via route B (nitridation) or route D (oxidation).

In this work, we have fabricated epitaxial TiN/TiNO thin films with a controlled oxidation process using PLD. Tailoring the properties of the TiNO system via controlled oxidation has an energy advantage over the conventional method of bandgap engineering of TiO_2 via nitridation.[40−43] The energy advantage comes from the higher activation energy of the nitridation process (672 kJ/mol) than that of the oxidation process (496 kJ/mol). The favorable energetics of an oxidation process coupled with the existence of an isostructural rock-salt phase between TiN (no oxygen substitution) and TiO (N fully substituted with O—see Figure 1) is anticipated to result in the realization of a much wider doping range of O into TiN than N into TiO_2. However, due to the absence of the isostructural phase between TiN and TiO_2, the substitutional nitrogen doping beyond 5.5 atomic % has not been realized when TiO_2 is subjected to nitridation.[44] The possibility of oxygen occupying an interstitial site in the TiN lattice instead of substituting the nitrogen is ruled out by the positive incorporation energy for the interstitial site (+1.59 eV) and negative incorporation energy (−3.54 eV) at the N substitutional site.[45] It is also worth noting that while the TiNO obtained via oxidation of TiN has Ti^{3+}cation vacancy defects, TiNO obtained via nitridation of TiO_2 has Ti^{3+} or Ti^{4+} cation interstitial defects. Therefore, the physiochemical properties of TiNO with the same elemental compositions obtained using the two routes might differ significantly.

2. EXPERIMENTAL DETAILS

TiN/TiNO thin films were prepared on *c*-plane (0001) sapphire substrates by a PLD (Excel Instruments Inc.) method using a commercially available 99.99% pure TiN target and a KrF laser (Coherent COMPexPro, $\lambda = 248$ nm, pulse duration 25 ns, 10 Hz repetition rate). Prior to the deposition, substrates were first cleaned with acetone and then with ethanol in a sonicating bath for 30−40 min to remove surface impurities. After mounting the substrate on the substrate holder, the PLD chamber was pumped down to a base pressure of $\sim 3 \times 10^{-6}$ T. Then, a laser fluence of 2.5 J/cm^2 was focused on the TiN target for deposition while maintaining the substrate temperature at 550 °C. The number of laser pulses varied from 150 to 5000, corresponding to film deposition times of 0.25−8.33 min. The thicknesses of these films, measured using optical profilometry (3D Surface Profiler, New VK-X3000) and/or x-ray reflectometry (XRR), were found to be 1.7, 2.5, 3.5, 5.2, 6.3, 12.5, 16.4, and 30.7 nm for films made using 150, 300, 500, 750, 1000, 3000, 4000, and 5000 laser pulses (P), respectively. The films were characterized using XRD, XRR, XPS, and UV−visible spectroscopy. An X-ray diffractometer (Bruker D8) was used to calculate the thicknesses of the TiN films from XRR curves utilizing the Bruker LEPTOS software (v7.10). The same diffractometer was used for lock-couple 2θ-θ, phi scans, and omega-rocking curve scans. XPS measurements were carried out using a Scienta Omicron ESCA 2SR with operating pressure $\sim 1 \times 10^{-9}$ T. Monochromatic Al Kα X-rays (1486.6 eV) were generated at 250 W with photoelectrons collected from a 2 mm-diameter analysis spot. XPS peaks were fitted using the CasaXPS software; the binding energy of the adventitious C 1s peak (at 284.8 eV) was used to calibrate the energy axis. Bandgaps were calculated from a combination of reflectance and transmission data measured on a Cary 5000 UV−Vis−NIR spectrophotometer in the wavelength range 200−800 nm, step size 1 nm, and scan rate 300 nm/minute. A DRA-2500 accessory with an integrating sphere was used to collect the total diffuse plus specular reflectance and to measure the total transmission. The integrating sphere is a spherical cavity whose inner wall is coated with a highly reflective material such as magnesium oxide and barium sulfate. In an integrating sphere, light undergoes multiple reflections so that the intensity of the light reaching the detector is angularly uniform.

To preserve the authenticity and reproducibility of data, we have randomly deposited a set of films three times under identical conditions. Their properties (thickness, FWHM, four-probe resistivity, bandgap, and XPS compositions) are then measured at least twice. Those measurements are used to establish the error bar for a particular data point. A more specific error analysis approach used for a particular technique is described in the appropriate section.

3. RESULTS AND DISCUSSION

XPS survey scans acquired after Ar ions cleaning showed core level lines originating from Ti (Ti 2s, Ti 2p, Ti 3s, Ti 3p), N 1s, and O 1s, as shown in Figure 2a. The presence of O 1s peaks at 530.6−531.4 eV highlighted the presence of oxynitride and oxide species (TiNO/TiO_2) in the samples. The oxidation of TiN to TiNO/TiO_2 is caused by the presence of residual oxygen in the PLD chamber.[20,29] The atomic percentages of Ti, N, and O in the thin-film samples are summarized in Table 1. The features observed at 1067.9 and 974.6 eV correspond to Ti LMM and O KLL Auger peaks, respectively.[46,47]

High-resolution spectra of Ti 2p core-level XPS peaks were also recorded (Ti 2p: 445−475 eV) to further detail the chemical state of the samples. Due to spin-orbit coupling, a doublet of Ti 2p peaks was noticed in the XPS spectra, Ti $2p_{3/2}$ and Ti $2p_{1/2}$. It is to be noted that the high reactivity of TiN

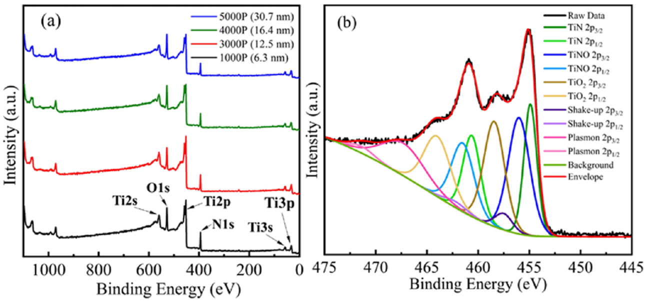

Figure 2. (a) XPS survey scan spectra (0−1100 eV) for TiNO thin films with different thicknesses prepared using 1000−5000 pulses (P) showing Ti (2s, 2p, 3s, 3p), O 1s, and N 1s peaks (no background subtraction performed); O 1s, Ti 2p, and N 1s peaks were identified at binding energies of 531.4, 455.4, and 397.4 eV for the highest thickness film prepared using 5000 laser pulses. For the TiNO film prepared using 1000 laser pulses, O 1s, Ti 2p, and N 1s peaks were identified at binding energies of 530.6, 454.6, and 396.6 eV. (b) Deconvolution of the high-resolution Ti 2p spectra for a 30.7 nm-thick film prepared using 5000 laser pulses after Ar^+ sputtering (including a Tougaard background).

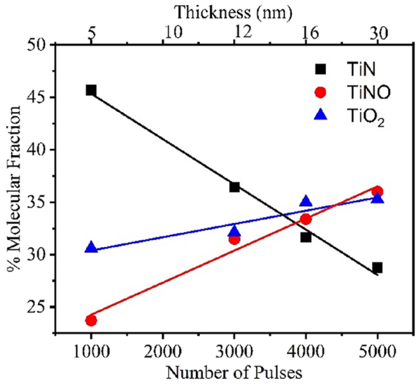

Figure 3. Molecular fractions of TiN, TiNO, and TiO_2 in the thin-film samples as a function of the number of pulses. The average variation in data was less than ±2%, which was determined from the data on three samples deposited using 1000 laser pulses.

toward oxygen often leads to the formation of TiNO and TiO_2. Thus, the Ti 2p spectra were deconvolved to correctly identify and account for TiNO and TiO_2 species in the samples shown in Figure 2b. For the samples measured using XPS, the peak positions of TiN $2p_{3/2}$, TiNO $2p_{3/2}$, and TiO_2 $2p_{3/2}$ matched well with the literature.[41,46,47] The gap between the 2p-doublet peaks ($2p_{3/2}$ and $2p_{1/2}$) of TiN, TiNO, and TiO_2 remained somewhat constant with an average of 5.79, 5.23, and 5.37 eV for samples made using 1000 to 5000 laser pulses. However, chemical shifts of the deconvolved peaks (to higher binding energies) were evident for samples with higher deposition times. For example, the TiN $2p_{3/2}$, TiNO $2p_{3/2}$, and TiO_2 $2p_{3/2}$ peaks demonstrated approximately 0.07, 0.14, and 0.09% increases in their binding energy, respectively, signaling a higher oxidation state of the samples. To avoid errors in XPS data and their analysis, the following care was taken: XPS spectra were recorded with low noise and a high peak-to-background ratio, selecting proper model function, reducing the number of free parameters by means of existing information on well-known doublet splitting and intensity ratios, running the fit procedure with Tougaard background subtraction, and checking the values of the residual standard deviation fittings. For example, the residual standard deviation for our XPS fittings is ~1.5 units (CPS), which is quite good.

The XPS percentage molecular fractions of TiN, TiNO, and TiO_2 are plotted against the number of laser pulses in Figure 3. As seen in this figure, the molecular fraction of TiN decreases by ~35% and the fraction of TiNO increases by 50% with an increase in the laser pulse from 1000 to 5000, while the variation of the molecular fraction of TiO_2 was much smaller (~15%). The near-time independent formation of TiO_2 is explained by considering the gas phase formation of TiO_2 due to the higher reactivity of titanium atoms/ions in the laser plume with residual oxygen than with nitrogen atoms. It should be noted that no oxygen or nitrogen was added to the chamber intentionally during any of the film depositions. The TiN thin film is oxidized on the substrate after its formation via a post-deposition time-dependent oxygen diffusion process in the presence of the atmosphere of residual oxygen. As a result, the net nitrogen content in the films decreases with increasing deposition time or number of pulses, while the O content increases with increasing number of pulses. This increase in oxygen percentage results in an increase in Ti−O and Ti−N−O bonding percentage and possibly modification of the chemical (and physical) state of the TiN/TiNO lattice. The chemical formulas of the TiNO film deposited using 1000 to 5000 laser pulses are listed in Table 1. An equivalent chemical formula is written to indicate the atomic fraction of oxygen that is in excess of oxygen atoms needed for the formation of TiNO in a rock-salt structure. For example, $TiN_{0.60}O_{1.09}$ (made using 5000 laser pulses) is alternatively written as $TiN_{0.60}O_{0.40\,+\,0.69}$. The first subscript number on O (0.40) stands for the fractional level of the substitution on the N positions, and the second number (0.69) stands for excess oxygen in the film.

Applying the general formula proposed for the TiNO homolog series described earlier in the introduction section, the molecular formula of this TiNO can be written as $Ti^{3+}_{1-0.4\ /3}Ti(vac)^{3+}_{0.4/3=0.13}N^{3-}_{(1-0.4=0.6)}O^{2-}_{0.4}$.The lattice is electri-

Table 1. Ti^{3+} **Defect Density Calculation from** $Ti^{3+}_{(1-x/3)}Ti(vac)^{3+}_{x/3}N^{3-}_{(1-x)}O^{2-}_{x}$[a]

	elemental percent			chemical formula			Ti^{3+} defect density per cm^3	
number of laser pulses	Ti	N	O	actual	equivalent (showing excess oxygen, O_{Excess})	Ti^{3+} vacancy per unit cell	total	actual (TiNO)
1000	40.06	29.25	30.69	$TiN_{0.73}O_{0.77}$	$TiN_{0.73}O_{0.27+0.50}$	0.09	1.19×10^{21}	2.82×10^{20}
3000	41.09	28.39	30.52	$TiN_{0.69}O_{0.74}$	$TiN_{0.69}O_{0.31+0.43}$	0.10	1.34×10^{21}	4.34×10^{20}
4000	40.30	25.04	34.66	$TiN_{0.62}O_{0.86}$	$TiN_{0.62}O_{0.38+0.48}$	0.13	1.63×10^{21}	5.43×10^{20}
5000	37.15	22.41	40.44	$TiN_{0.60}O_{1.09}$	$TiN_{0.60}O_{0.40+0.69}$	0.13	1.64×10^{21}	5.88×10^{20}

[a] The average variation in elemental composition data was less than ±2%, which was determined from the data on three samples deposited using 1000 laser pulses.

cally neutral following the departure of 0.13 Ti^{3+} cations per lattice, which combine with 0.69 O^{2-} to form stoichiometric TiO_2 ($Ti_{0.13}O_{0.26}$) or non-stoichiometric titanium dioxide. The excess oxygen (0.69−0.26 = 0.43) can form O_2 or bond with H to generate O−H bonds; the O−H bonds were indeed observed in the XPS O 1s peaks. The actual Ti^{3+} defect density shown in Table 1 was calculated by multiplying the total Ti^{3+} defect density estimated from the charge balance formula with the molecular fraction of TiNO obtained from XPS (Figure 3).

XRD patterns were recorded for all TiNO films, which showed that (111) was the preferred orientation; a 2θ-θ XRD pattern of a representative TiNO film made using 5000 laser pulses is shown in Figure 4a. The peak positions matched with JCPDS (JCPDS: 00-038-1420) data of the rock-salt structure. The crystalline quality of the samples was evaluated by omega-rocking curve analysis (inset of Figure 4a). The full width at half maxima (FWHM) values (measured from the rocking curves) were narrow, ∼0.033° to 0.046°, indicating the high crystalline quality of the films. However, higher FWHM values for samples made using a high number of pulses indicated decreasing crystallinity. This may be attributed to an increase in the defect density with an increase in the number of pulses from 1000 to 5000 (Table 1). Lattice constants for the TiNO films were found to be 4.23, 4.26, 4.27, and 4.30 Å for films made using 1000, 3000, 4000, and 5000 laser pulses, respectively.

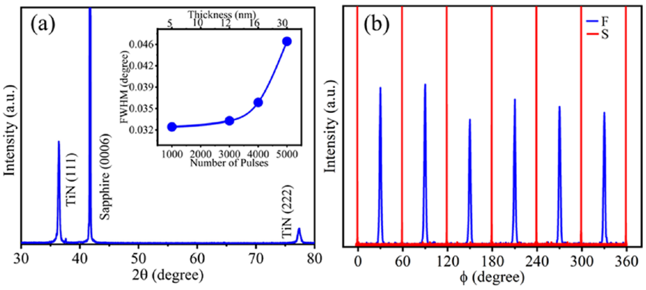

Figure 4. (a) XRD pattern for a TiNO thin film made using 5000 laser pulses. (Inset) FWHM values of the (111) peak versus the number of laser pulses; the solid line is a guide to the eye. (b) ϕ scan of the 5000-pulse sample showing sapphire substrate (113)—S and TiNO film (200)—F peaks. The average variation in FWHM data was less than ±1%, which was determined from the data on three samples deposited using 1000 laser pulses.

The degree of in-plane alignment was determined using phi (ϕ) scans of the TiNO film and sapphire substrate with the rotation axis perpendicular to the film thickness (Figure 4b). Sapphire shows a characteristic sixfold symmetry with a 60° spacing of diffraction peaks.[26,48] The appearance of TiN film peaks spaced at 60° in the ϕ-scan also suggested a sixfold symmetry of TiN thin films instead of threefold symmetry, which can be explained based on TiN grain formation with a twin structure.[49] The ϕ-scan peaks of the TiN films were relatively wider than the peaks for the single-crystal sapphire substrate, which hints at disorder near the interface in the TiN films.[48,49]

To understand the origin of lattice expansion with increasing O content in the films, we performed molecular dynamics (MD) simulations of isolated point defects in bulk TiN and TiNO. The open-source MD code LAMMPS[50] was used for all simulations, and OVITO[51] was used to visualize the atomic trajectories. Atomic interactions were modeled using the COMB3 potential parameterized for TiNO.[52−54] The COMB3 potential function was chosen for its relative computational efficiency over ab initio methods and its ability to model larger systems. While COMB3 does not explicitly include electrons, a Coulombic force term is included. COMB3 also allows for charge redistribution and charge equilibration due to changes in the local atomic structure and electronegativity differences between different element types. Defect energies calculated with the COMB3 potential by

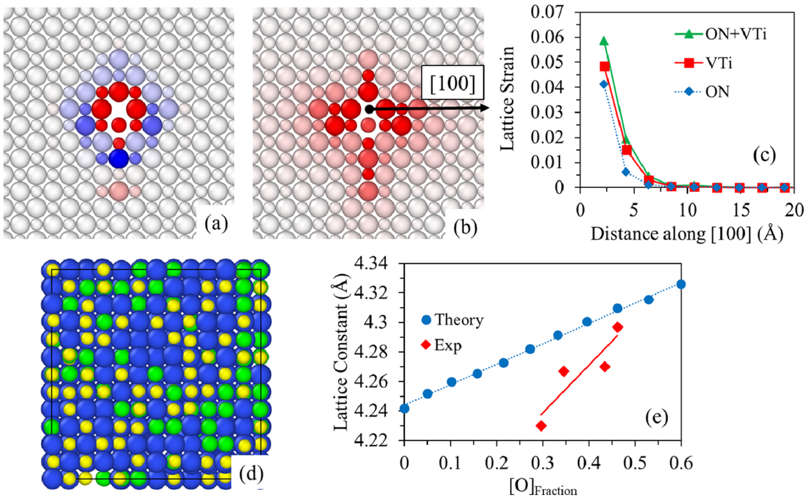

Figure 5. (a) The (001) plane of atoms containing V_{Ti} + O_N defect with atoms color-coded by the change in atomic charge (Δq) relative to the perfect TiN lattice, with a color gradient having red spheres $\Delta q = +0.1$, white $\Delta q = 0$, and blue $\Delta q = -0.1$ in units of elemental charge (e). (b) The same atoms colored by the magnitude of the displacement vector $|\Delta \vec{R}|$ relative to the perfect TiN lattice with the color gradient ranging between red $|\Delta \vec{R}| = 0.05$ Å and white 0 Å. (c) Plot of lattice strain along the [100] axis. (d) A representative snapshot of the atomic configuration of bulk TiNO ($TiN_{0.82}O_{0.27}$) after energy minimization. Atoms are colored by type (Ti = yellow, N = blue, O = green). (e) Lattice constant as a function of [O] fraction for the simulation data (blue circles) and experimental data obtained by (XRD) (red diamonds). For the experimental data, $[O]_{fraction} = [O]_{total} - [O]_{excess}$, as given in Table 1. In each atomic snapshot, spheres representing Ti^{3+}, N^{3-}, and O^{2-} ions are scaled by their corresponding ionic radius: 0.81, 1.32, or 1.0 Å.

https://doi.org/10.1021/acsami.2c18926

Cheng et al. yield similar trends to density functional theory (DFT), although the incorporation energies tend to have a larger magnitude relative to the reported DFT values.[52] This gives confidence that the COMB3 potential captures the correct physics with respect to defect configurations. Cheng et al. mentioned that the magnitudes of defect formation energies are generally larger than those from DFT due to compromises made during the parameterization of the potential function that prioritized cohesive energy and phase ordering.[52]

To determine the minimum energy configuration of TiN point defects and bulk TiNO structures in our simulations, a simulated annealing approach was employed. In this procedure, the atoms were assigned an initial temperature of 10 K. The trajectories of the atoms progress in an isoenthalpic−isobaric ensemble. An MD time step size of 0.5 fs was applied. A viscous damping term of 0.01 eV ps $Å^{-2}$ was added to slowly remove kinetic energy from the system during the annealing process. The system is assumed to have arrived at a minimum energy configuration after 10,000 MD steps, at which point the change in total energy was generally less than 10^{-6} eV/step.

A periodic cubic cell containing 11 × 11 × 11 unit cells of a TiN lattice in the rock-salt structure was used to investigate the lattice strains in the neighborhood of isolated Ti vacancies (V_{Ti}), O substituted on N sites (O_N), and combined V_{Ti} + O_N point defects. The number of unit cells was chosen to be sufficiently large so that defects in periodic images of the original cell do not interact. The minimum energy structures are obtained before and after the introduction of the defect so that changes in per atom charges and atomic displacements can be mapped relative to the original lattice.

Figure 5a shows the change in per-atom charge relative to a V_{Ti} + O_N point defect relative to the perfect TiN lattice. Atoms have been colored by the change in charge (Δq) with a color gradient, blue being −0.1, white being neutral, and red being +0.1 in units of elemental charge, e. In Figure 5a, the simulation cell has been sectioned such that only atoms lying on the (001) plane containing the defect are shown. Atoms are drawn to scale according to their respective ionic radii (0.81, 1.32, or 1.0 Å for Ti, N, or O, respectively). The Δq on atoms immediately surrounding the Ti vacancy becomes more positive because the Ti atom is no longer present to donate electron density to the more electronegative N or O anions that surround the Ti lattice site. Atoms one to two lattice distances from the defect center become more negative as they donate some of their electron density to the atoms in the immediate vicinity of the defect. Δq decays to near zero at distances greater than three lattice units from the defect. Figure 5b shows the magnitude of the lattice expansion relative to the initial perfect lattice, $|\Delta \vec{R}|$. Here, the gradient from red to white indicates $|\Delta \vec{R}|$ ranging from 0.05 to 0 Å. This lattice expansion can be explained in terms of the relative changes in charges surrounding the defect. The positive Δq on atoms adjacent to the defect center is no longer counterbalanced by neighboring Ti atoms and causes an electrostatic repulsion. At the same time, the negative Δq on atoms one to two lattice units away from the defect causes an electrostatic attraction and pulls the inner atoms further from the defect center. The net result is a displacement of atoms away from the defect center, which results in local lattice expansion surrounding the defect. The lattice strain along the x = [100] direction, as indicated by the vector superimposed in Figure 5b, is shown in Figure 5c for V_{Ti} + O_N, V_{Ti}, and O_N defects. The lattice strain in the [100] direction is calculated as $\Delta x/x_0$, where Δx is the change in atom position relative to the perfect lattice and x_0 is the position of the atom in the perfect lattice. The strain is greatest in the immediate vicinity of the defect, ranging between +4 and +6% depending on the defect type. The strain field decays rapidly as the distance from the defect center increases. Thus, the increase in V_{Ti} as required to maintain overall charge neutrality with increasing O_N can be used to explain the experimentally observed increase in lattice constant with increasing O concentration.

To further test this hypothesis, we have simulated bulk TiNO at different O:N ratios. Starting from a 6 × 6 × 6 unit cell block of TiN in the rock-salt structure, we randomly substitute a given fraction of N sites for O. To maintain charge neutrality, one Ti atom is randomly removed for every three O for N substitutions. For example, in the 6 × 6 × 6 unit cell block, there are 1748 total atoms, half of which (864) are N. If 25% of the N is randomly replaced with O, 216 O atoms are added, leaving 648 N atoms in the lattice. To maintain charge neutrality, 72 Ti atoms must also be removed. Applying the formula in Table 1 yields a chemical formula of $TiN_{0.82}O_{0.27}$ for this example. After the initial structure is generated, the minimum energy configuration is determined using the isobaric−isoenthalpic thermal annealing algorithm described above. The volume of the resulting system is used to calculate the lattice constant of the resulting structure according to $a_0 = \sqrt[3]{V}/6$, where V is the final total volume of the simulation cell after equilibration and 6 is the number of unit cells in each direction. Shown in Figure 5d is the minimum energy configuration for $TiN_{0.82}O_{0.27}$. Atoms are colored by type, with Ti = yellow, N = blue, and O = green. As before, atoms are scaled by their respective ionic radii. The original rock-salt structure is maintained upon the addition of O to the lattice. This process was repeated for N:O ratios varying between 0 and 0.5 (corresponding formula units from TiN to $TiN_{0.6}O_{0.6}$). The resulting lattice constant as a function of $[O]_{fraction}$ is plotted in Figure 5e. To test for consistency in the simulation results, the lattice constant was calculated for five different random starting configurations for $[O]_{fraction}$ = 0.6, which represents the largest compositional variation tested relative to the ideal TiN structure. The associated error was too small to be shown when plotted in Figure 5e. Satisfied that the variation was small, no additional simulations were run. For comparison, the experimental lattice constants obtained via XRD for samples prepared with 1000, 3000, 4000, and 5000 laser pulses have been plotted alongside the simulation data. For this graph, the O concentration for the experimental data was adjusted to fit the simulation data according to $[O]_{fraction} = [O]_{total} - [O]_{excess}$, as expressed in Table 1. Experiment and theory show similar trends in that the lattice constant increases with increasing O in the film. This result tends to support the theoretical explanation that the electrostatic interactions in the vicinity of V_{Ti} described above leads to lattice expansion in TiNO with increasing O composition. The rate of increase in lattice constant with respect to $[O]_{fraction}$ varies considerably between theory and experiment. This may be attributed to the fact that the current model does not include excess O in the form of TiO_2 or O_2 incorporated into the film. The development of a more detailed model that includes TiNO, TiO_2, and O_2 will be left to future work.

The modified chemical state and structure of the TiN/TiNO thin films have been found to strongly impact the optoelectronic properties of the samples, as reflected by their bandgap data presented in Figure 6. The bandgap measurements were carried out using a UV−vis diffuse reflectance spectrophotometer coupled with an integrating sphere. It should be noted that a diffuse reflectance is ideally suited for powder samples where the optical angle of incidence ≠ angle of reflection). The smooth, shiny, and epitaxial thin-film samples, such as in the present study, mostly reflect the incident light specularly, where the angle of incidence = angle of reflection. Such thin-film samples can be analyzed either in diffuse reflectance or in specular reflectance mode. A standard light trap, mounted at the specular reflectance angle on the internal surface of the integrating spheres, allows the measurement of the diffuse component only. On the other hand, in the present study, our system is capable of only mounting a white specular plate at the specular reflectance angle on the internal surface of the integrating sphere. Thus, all the UV measurements in this study involve data collection in the total reflectance mode.

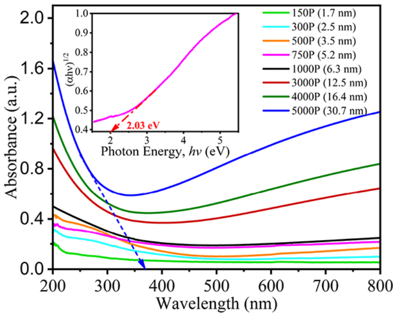

Figure 6. Absorbance as a function of wavelength for the TiNO thin films made using 150 to 5000 laser pulses. The blue dashed line (tangent) points to the absorption wavelength (368 nm) of the sample made using 5000 laser pulses (30.7 nm). (Inset) An example of the bandgap estimation (2.03 eV) using the Tauc plot for a TiNO film made using 750 laser pulses (5.2 nm thick).

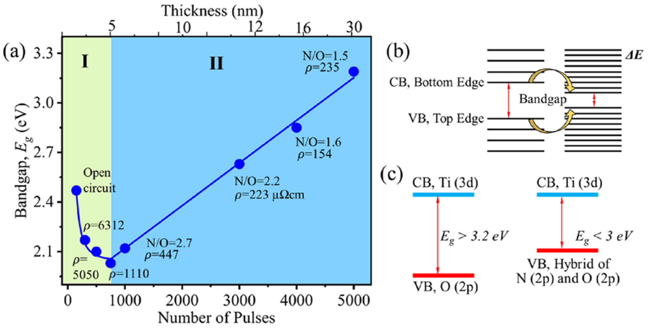

Figure 7. (a) Bandgap of TiN/TinO samples as a function of the number of pulses; the solid line is a guide to the eye. (b) Schematic of size effect on the bandgap increase and energy states (ΔE) separation (left: bigger particle, right: smaller particle). (c) Schematic of bandgap reduction due to hybridized valence band made of O_{2p} and N_{2p} orbitals (left: pure O_{2p} orbital, right: hybridized O_{2p} and N_{2p} orbitals). The average variations in bandgap and resistivity data were less than ±2 and 5%, respectively, which was determined from the data on three samples deposited using 1000 laser pulses.

The bandgap excitation wavelength values were noted from the x-axis intercepts of the tangents at the point of inflection on the absorbance curves (before the curve minimum from the origin side). As seen in Figure 6, the absorption wavelength needed for the electronic excitation from the valence band to the conduction band decreases from 490 nm (away from blue light) to 368 nm (more toward blue light) as the film thickness changes from 6.3 to 30.7 nm. The decrease in the wavelength of the absorption light is termed as blueshift. However, the values of the tangent intercepts for lower-thickness films indicate that the blueshift trend is reversed (called negative blue shift or redshift), i.e., the absorption wavelength increases from 506 nm (more toward blue light) to 617 nm (away from blue light). These opposite optical properties of thinner and thicker samples are also reflected in Figure 7. The bandgap of the samples was calculated using eq 1 for an indirect semiconductor from the Tauc plot, which is used in the case of composite samples consisting of mixed phases.[55−58] In the case of a direct bandgap semiconductor, the left side term has an exponent value of 2.[55] The XPS data on our samples have indicated the presence of TiO_2, TiNO, and TiN.

$$(\alpha h\upsilon)^{1/2} \propto (h\upsilon - E_g) \qquad (1)$$

where h is Planck's constant, υ is the photon's frequency, α is the absorption coefficient, and E_g is the bandgap. By plotting $(\alpha h\upsilon)^{1/2}$ against photon energy ($h\upsilon$) and through extrapolating the linear part of the $(\alpha h\upsilon)^{1/2}$ curve to zero, the optical bandgaps of TiN films were obtained according to the Tauc plot.[25,57] A representative plot of $(\alpha h\upsilon)^{1/2}$ vs $h\upsilon$ is displayed in the Figure 6 inset for the sample made using 750 laser pulses.

As shown in Figure 7a, the optical bandgap of the TiN/TiNO films showed a strong dependence on the film thickness. The data points in Figure 7a are also marked with their electrical resistivity that varied from 6312 to 232 $\mu\Omega$cm for samples prepared using 150 to 5000 laser pulses, respectively. The data points are also marked with the corresponding N/O ratios obtained from the XPS measurements. The V-shaped variation of the bandgap as a function of the number of laser pulses is explained by dividing the curve into two regions, marked I and II. In region I, films are made using laser pulses from 150 to 750 pulses, which correspond to the time of deposition from 15 to 75 s. The thicknesses of these films are 1.7 nm (∼4 TiN lattice constants thick) to 5.2 nm (∼12 TiN lattice constants thick), as shown on the top x-axis of this figure. The TiN films are believed to be negligibly oxidized in region I due to a lack of surface oxidation at the base pressure of 3×10^{-6} T.[59,60] These films are non-continuous and can be regarded as zero-dimensional islands indicating the TiN film formation via the Volmer−Weber Island mechanism where adatom−adatom interactions are stronger than those of the adatom with the surface.[61,62] The resistivity of the TiN made using 150 laser pulses is in the range of several mega ohms; it is practically immeasurable by a voltmeter. The first measured resistivity value is 6312 $\mu\Omega$cm, which is for the TiN film made using 300 laser pulses. The TiN film made using 750 laser pulses marks the transition of region I to region II, i.e., the transition from 0D non-continuous oxygen-free TiN films (or negligibly oxidized TiN films due to high time constant of TiN to TiNO reaction) to partially oxidized 2D continuous TiN films. The resistivity of partially oxidized TiN films, i.e., TiNO films, decreases continuously with an increase in film thickness. It may be noted that a trustworthy experimental evidence about the absence of TiNO phase using XPS cannot be obtained since the thinner films were not fully covering the substrate, and hence, a large portion of the oxide substrate was uncovered. However, the TiN films, even with these small thicknesses, would be interspersed with a small fraction of

TiO_2 formed in the laser plume due to the high reactivity of Ti with oxygen. Using the linear variation of the TiO_2 fraction with laser pulses, the fraction of the TiO_2 phase in the films made using 150 to 750 laser pulses is extrapolated to be 4 to 6%.

In region I, the bandgap of the 0D non-continuous TiN films increases gradually from 2.03 to 2.47 eV with decreasing number of laser pulses used to make them. This behavior is attributed to the size effect of islands in an almost non-continuous thin-film structure. Applying the idea of the density of states and the Fermi function in region I, it can be shown that $E_g \propto \frac{N_E}{D^3}$ and $\Delta E \propto \frac{1}{D^3}$.[63,64] As shown schematically in Figure 7b, the separation between energy states (ΔE) and the separation between the valence and conduction band (i.e., bandgap, E_g) increase with a reduction in the island dimension (D). If ΔE is more than E_g, the excitation of an electron from the valence band to the conduction band is restricted and unoxidized TiN films, which should have ideally behaved metallic, start exhibiting high resistivity and semiconductor characteristics.[65]

Applying the quantum confinement effect, the bandgap energy of the TiN films made using 150 to 750 laser pulses was fitted to the following equation:[66−69]

$$E_g = E_{g,\mathrm{bulk}} + B/t^2 \qquad (2)$$

,where $E_{g,\mathrm{bulk}}$ is the band gap energy of the bulk TiN crystal, B is the quantum confinement constant, and t is the thickness of the TiN films. As seen in Figure 8, the bandgap energy data fits well with eq 2 with the goodness of the fitting (R^2) value close to unity (0.99) and a low reduced chi-square (χ^2) value was 3.6×10^{-4}. From this fitting, the values of $E_{g,\mathrm{bulk}}$ and B were found to be 1.96 and 1.45 eV nm^2, respectively; $E_{g,bulk}$ agreed well with the bandgap value of bulk TiN.[58]

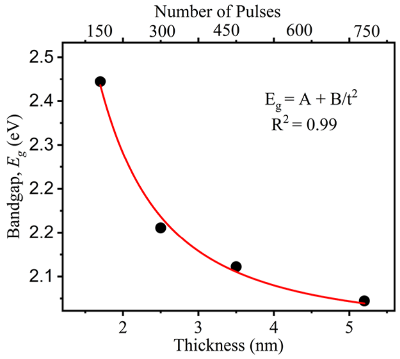

Figure 8. Bandgap as a function of thickness for the TiN films made using 150 to 750 laser pulses, and the solid curve is a fit to the quantum confinement model.

In region II, the bandgap increased from 2.03 to 3.21 eV for TiN films made using 1000 to 5000 laser pulses. As is evident from XPS results, the TiN films in region II, made using a significantly higher number of laser pulses, are all partially oxidized (and should be more correctly called TiNO) but still have the rock-salt lattice structure. As the number of laser pulses increases, the TiN films have more time for oxidation via surface diffusion of the residual oxygen in the deposition chamber to the TiN films. Consequently, O content in the TiNO films increases with increased laser pulses. In other words, N/O increases with a decrease in the laser pulses. The decrease in TiNO bandgap values with a decrease in the laser pulses (or a decrease in the N/O ratio) is explained on the basis of the partial substitution of nitrogen by oxygen. When N atoms in TiN are partially substituted by O atoms, the top of the valence band consists of hybridized orbitals of O_{2p} and N_{2p}. Since the energy of N_{2p} is higher than that of O_{2p}, the valence band maximum in the oxynitride system is located at higher potential energy than that for pure TiO_2 due to the contribution of N_{2p} orbitals, as shown in Figure 7c.[55,70] The bandgap of the resulting TiNO compound, as evident from the experimental data in Figure 7a, has been tuned to lower than 3.5 eV enabling them to respond to visible solar light.

4. CONCLUSIONS

A systematic study was carried out to understand the effects of elemental chemical states and structural phases in TiN/TiNO thin films on their electrical and optical properties. XPS survey scans and deconvolution of high-resolution scans were used to identify the increased presence of TiNO and TiO_2 species in the samples made using large numbers of pulses, i.e., higher thickness. The modified chemical composition and structural properties of the TiNO thin films were found to cause a V-shaped variation of bandgap with respect to the number of pulses. The increasing bandgap of the ultra-thin films' (made using less than 750 laser pulses) was attributable to the size effect. Thin films made using more than 750 laser pulses were more prone to oxidation, which resulted from an increase in the bandgap. The study suggests that the TiN/TiNO thin-film system is a promising photoelectrocatalyst, electrocatalyst, and non-carbon support material needed in clean energy and water-splitting research.

■ AUTHOR INFORMATION

Corresponding Author

Dhananjay Kumar − *Department of Mechanical Engineering, North Carolina A&T State University, Greensboro, North Carolina 27411, United States;* orcid.org/0000-0001-5131-5131; Email: dkumar@ncat.edu

Authors

Manosi Roy − *Department of Mechanical Engineering, North Carolina A&T State University, Greensboro, North Carolina 27411, United States;* orcid.org/0000-0002-8119-3304
Kaushik Sarkar − *Department of Mechanical Engineering, North Carolina A&T State University, Greensboro, North Carolina 27411, United States;* orcid.org/0000-0002-4031-4800
Jacob Som − *Department of Mechanical Engineering, North Carolina A&T State University, Greensboro, North Carolina 27411, United States*
Mark A. Pfeifer − *Cornell Center for Materials Research, Cornell University, Ithaca, New York 14850, United States*
Valentin Craciun − *National Institute for Laser, Plasma and Radiation Physics, Magurele 077125, Romania*
J. David Schall − *Department of Mechanical Engineering, North Carolina A&T State University, Greensboro, North Carolina 27411, United States;* orcid.org/0000-0002-3694-9934
Shyam Aravamudhan − *Joint School of Nanoscience and Nanoengineering, North Carolina A&T State University, Greensboro, North Carolina 27401, United States;* orcid.org/0000-0001-9968-7188

Frank W. Wise − *Cornell Center for Materials Research, Cornell University, Ithaca, New York 14850, United States*

Complete contact information is available at: https://pubs.acs.org/10.1021/acsami.2c18926

Author Contributions

M.R.: data curation (lead); methodology (lead); writing original draft (lead), writing—review and editing, analysis. K.S.: methodology (supporting). J.S.—methodology (supporting). M.A.P.: data curation. V.C.: writing—review and editing; analysis. J.D.S.: writing—original draft (supporting), review and editing, analysis. S.A.: writing—review and editing. F.W.W.: writing—review and editing. D.K.: conceptualization (lead); funding acquisition (lead); supervision; writing—original draft (equal); writing—review and editing (equal), analysis.

Notes

The authors declare no competing financial interest.

ACKNOWLEDGMENTS

The authors would like to acknowledge the NSF-PREM grant (DMR-2122067), which was the primary source of financial and infrastructural support for this research. This work was partially supported by the Cornell Center for Materials Research and made use of the CCMR Shared Facilities, which are supported by the NSF MRSEC program (DMR-1719875). The authors acknowledge the assistance of Darrah Dare in the XPS measurements. The authors would like to thank NCAT Joint School of Nanoscience and Nanoengineering, a member of the Southeastern Nanotechnology Infrastructure Corridor (SENIC) and National Nanotechnology Coordinated Infrastructure (NNCI), which is supported by the National Science Foundation (ECCS-2025462). V.C. was partially supported by the Romanian Nucleu Programme LAPLAS VI, no. 16 N/2019.

REFERENCES

(1) Matsuoka, M.; Kitano, M.; Takeuchi, M.; Tsujimaru, K.; Anpo, M.; Thomas, J. M. Photocatalysis for New Energy Production: Recent Advances in Photocatalytic Water Splitting Reactions for Hydrogen Production. *Catal. Today* **2007**, *122*, 51−61.

(2) Jiao, Y.; Zheng, Y.; Jaroniec, M.; Qiao, S. Z. Design of Electrocatalysts for Oxygen-and Hydrogen-Involving Energy Conversion Reactions. *Chem. Soc. Rev.* **2015**, *44*, 2060−2086.

(3) Seh, Z. W.; Kibsgaard, J.; Dickens, C. F.; Chorkendorff, I.; Nørskov, J. K.; Jaramillo, T. F. Combining Theory and Experiment in Electrocatalysis: Insights into Materials Design. *Science* **2017**, *355*, No. eaad4998.

(4) Seitz, L. C.; Dickens, C. F.; Nishio, K.; Hikita, Y.; Montoya, J.; Doyle, A.; Kirk, C.; Vojvodic, A.; Hwang, H. Y.; Norskov, J. K.; Jaramillo, T. F. A Highly Active and Stable IrOx/$SrIrO_3$ Catalyst for the Oxygen Evolution Reaction. *Science* **2016**, *353*, 1011−1014.

(5) Ahmed, M.; Xinxin, G. A Review of Metal Oxynitrides for Photocatalysis. *Inorg. Chem. Front.* **2016**, *3*, 578−590.

(6) Chappé, J.-M.; Martin, N.; Lintymer, J.; Sthal, F.; Terwagne, G.; Takadoum, J. Titanium Oxynitride Thin Films Sputter Deposited by the Reactive Gas Pulsing Process. *Appl. Surf. Sci.* **2007**, *253*, 5312−5316.

(7) Gebauer, C.; Fischer, P.; Wassner, M.; Diemant, T.; Jusys, Z.; Hüsing, N.; Behm, R. J. Performance of Titanium Oxynitrides in the Electrocatalytic Oxygen Evolution Reaction. *Nano Energy* **2016**, *29*, 136−148.

(8) Graciani, J.; Hamad, S.; Sanz, J. F. Changing the Physical and Chemical Properties of Titanium Oxynitrides $TiN_{1-x}O_x$ by Changing the Composition. *Phys. Rev. B* **2009**, *80*, 184112.

(9) Venkataraj, S.; Severin, D.; Mohamed, S. H.; Ngaruiya, J.; Kappertz, O.; Wuttig, M. Towards Understanding the Superior Properties of Transition Metal Oxynitrides Prepared by Reactive DC Magnetron Sputtering. *Thin Solid Films* **2006**, *502*, 228−234.

(10) An, L.; Xia, Z.; Chen, P.; Xia, D. Layered Transition Metal Oxynitride $Co_3Mo_2O_x N_{6-x}$/C Catalyst for Oxygen Reduction Reaction. *ACS Appl. Mater. Interfaces* **2016**, *8*, 29536−29542.

(11) Pan, C.; Takata, T.; Kumamoto, K.; Ma, S. S. K.; Ueda, K.; Minegishi, T.; Nakabayashi, M.; Matsumoto, T.; Shibata, N.; Ikuhara, Y. Band Engineering of Perovskite-Type Transition Metal Oxynitrides for Photocatalytic Overall Water Splitting. *J. Mater. Chem. A* **2016**, *4*, 4544−4552.

(12) Wang, S.; Li, L.; Shao, Y.; Zhang, L.; Li, Y.; Wu, Y.; Hao, X. Transition-Metal Oxynitride: A Facile Strategy for Improving Electrochemical Capacitor Storage. *Adv. Mater.* **2019**, *31*, 1806088.

(13) Sarker, N. R.; Cherukupally, P.; Gourevich, I.; Wilbur, J.; Jons, S. D.; Bilton, A. M. Multi-Scale Visualization of Incipient $CaCO_3$ Scaling on the Polyamide Layer of Reverse Osmosis Membranes. *Desalination* **2022**, *539*, 115956.

(14) Archer, M. D. Photovoltaics and Photoelectrochemistry: Similarities and Differences. *Physica E: Low-dimensional Systems and Nanostructures.* **2002**, *14*, 61−64.

(15) Kudo, A. Z-Scheme Photocatalyst Systems for Water Splitting under Visible Light Irradiation. *MRS Bull.* **2011**, *36*, 32−38.

(16) Windle, C. D.; Kumagai, H.; Higashi, M.; Brisse, R.; Bold, S.; Jousselme, B.; Chavarot-Kerlidou, M.; Maeda, K.; Abe, R.; Ishitani, O.; Artero, V. Earth-Abundant Molecular Z-Scheme Photoelectrochemical Cell for Overall Water-Splitting. *J. Am. Chem. Soc.* **2019**, *141*, 9593−9602.

(17) Zhang, J. Z. Metal Oxide Nanomaterials for Solar Hydrogen Generation from Photoelectrochemical Water Splitting. *MRS Bull.* **2011**, *36*, 48−55.

(18) Fuertes, A. Nitride Tuning of Transition Metal Perovskites. *APL Mater.* **2020**, *8*, No. 020903.

(19) Hojamberdiev, M.; Kawashima, K. Exploring Flux-Grown Transition Metal Oxynitride Perovskites for Photocatalytic Water Oxidation: A Minireview. *Energy Reports.* **2020**, *6*, 13−24.

(20) Mucha, N. R.; Som, J.; Choi, J.; Shaji, S.; Gupta, R. K.; Meyer, H. M.; Cramer, C. L.; Elliott, A. M.; Kumar, D. High-Performance Titanium Oxynitride Thin Films for Electrocatalytic Water Oxidation. *ACS Appl. Energy Mater.* **2020**, *3*, 8366−8374.

(21) Ghailane, A.; Oluwatosin, A. O.; Larhlimi, H.; Hejjaj, C.; Makha, M.; Busch, H.; Fischer, C. B.; Alami, J. Titanium Nitride, $Ti_xN_{(1-x)}$, Coatings Deposited by Hipims for Corrosion Resistance and Wear Protection Properties. *Appl. Surf. Sci.* **2022**, *574*, 151635.

(22) Di, J.; Zhu, H.; Xia, J.; Bao, J.; Zhang, P.; Yang, S.-Z.; Li, H.; Dai, S. High-Performance Electrolytic Oxygen Evolution with a Seamless Armor Core−Shell Feconi Oxynitride. *Nanoscale* **2019**, *11*, 7239−7246.

(23) Som, J.; Choi, J.; Zhang, H.; Reddy Mucha, N.; Fialkova, S.; Mensah-Darkwa, K.; Suntivich, J.; Gupta, R. K.; Kumar, D. Effect of Substrate-Induced Lattice Strain on the Electrochemical Properties of Pulsed Laser Deposited Nickel Oxide Thin Film. *Mater. Sci. Eng., B* **2022**, *280*, 115711.

(24) Sarkar, K.; Jaipan, P.; Choi, J.; Haywood, T.; Tran, D.; Mucha, N. R.; Yarmolenko, S.; Scott-Emuakpor, O.; Sundaresan, M.; Gupta, R. K.; Kumar, D. Enhancement in Corrosion Resistance and Vibration Damping Performance in Titanium by Titanium Nitride Coating. *SN Appl. Sci.* **2020**, *2*, 949.

(25) Roy, M.; Kumar, D.Blue Shift in Ultraviolet Absorption Spectra of Oxygen Doped Titanium Nitride Thin Films. *ASME 2020 International Mechanical Engineering Congress and Exposition.*2020.

(26) Roy, M.*Growth, Structural, and Electrical Properties of TiN Thin Films, North Carolina Agricultural and Technical State University*. 2018.

(27) Sherman, A. Growth and Properties of LPCVD Titanium Nitride as a Diffusion Barrier for Silicon Device Technology. *J. Electrochem. Soc.* **1990**, *137*, 1892.

(28) Naik, G. V.; Schroeder, J. L.; Ni, X.; Kildishev, A. V.; Sands, T. D.; Boltasseva, A. Titanium Nitride as a Plasmonic Material for

Visible and Near-Infrared Wavelengths. *Opt. Mater. Express* **2012**, *2*, 478−489.

(29) Mucha, N. R.; Som, J.; Shaji, S.; Fialkova, S.; Apte, P. R.; Balasubramanian, B.; Shield, J. E.; Anderson, M.; Kumar, D. Electrical and Optical Properties of Titanium Oxynitride Thin Films. *J. Mater. Sci.* **2020**, *55*, 5123−5134.

(30) Martínez-Ferrero, E.; Sakatani, Y.; Boissière, C.; Grosso, D.; Fuertes, A.; Fraxedas, J.; Sanchez, C. Nanostructured Titanium Oxynitride Porous Thin Films as Efficient Visible-Active Photocatalysts. *Adv. Funct. Mater.* **2007**, *17*, 3348−3354.

(31) Livraghi, S.; Chierotti, M. R.; Giamello, E.; Magnacca, G.; Paganini, M. C.; Cappelletti, G.; Bianchi, C. Nitrogen-Doped Titanium Dioxide Active in Photocatalytic Reactions with Visible Light: A Multi-Technique Characterization of Differently Prepared Materials. *J. Phys. Chem. C* **2008**, *112*, 17244−17252.

(32) Mucha, N. R.; Roy, M.; Nannuri, C. S. R.; Kumar, D.; Rathnayake, H. Bandgap Engineering of Oxinitride Nanowires for Water Splitting and Hydrogen Generation. *APS March Meeting Abstracts* **2018**, G60−G311.

(33) Hussain, A. A.; Sharma, B.; Barman, T.; Pal, A. R. Self-Powered Broadband Photodetector Using Plasmonic Titanium Nitride. *ACS Appl. Mater. Interfaces* **2016**, *8*, 4258−4265.

(34) An, S.; Liao, Y.; Kim, M. Flexible Titanium Nitride/Germanium-Tin Photodetectors Based on Sub-Bandgap Absorption. *ACS Appl. Mater. Interfaces* **2021**, *13*, 61396−61403.

(35) El-Rahman, A. M. A.; Mohamed, S. H.; Khan, M. T.; Awad, M. A. Plasmonic Performance, Electrical and Optical Properties of Titanium Nitride Nanostructured Thin Films for Optoelectronic Applications. *J. Mater. Sci.: Mater. Electron.* **2021**, *32*, 28204−28213.

(36) Reddy, H.; Guler, U.; Kudyshev, Z.; Kildishev, A. V.; Shalaev, V. M.; Boltasseva, A. Temperature-Dependent Optical Properties of Plasmonic Titanium Nitride Thin Films. *ACS Photonics* **2017**, *4*, 1413−1420.

(37) Singh, A.; Li, X.; Protasenko, V.; Galantai, G.; Kuno, M.; Xing, H.; Jena, D. Polarization-Sensitive Nanowire Photodetectors Based on Solution-Synthesized CdSe Quantum-Wire Solids. *Nano Lett.* **2007**, *7*, 2999−3006.

(38) Lee, K.; Bharadwaj, S.; Shao, Y.-T.; van Deurzen, L.; Protasenko, V.; Muller, D. A.; Xing, H. G.; Jena, D. Light-Emitting Diodes with AlN Polarization-Induced Buried Tunnel Junctions: A Second Look. *Appl. Phys. Lett.* **2020**, *117*, No. 061104.

(39) Chaudhuri, R.; Bader, S. J.; Chen, Z.; Muller, D. A.; Xing, H. G.; Jena, D. A Polarization-Induced 2D Hole Gas in Undoped Gallium Nitride Quantum Wells. *Science* **2019**, *365*, 1454−1457.

(40) Avasarala, B.; Haldar, P. Electrochemical Oxidation Behavior of Titanium Nitride Based Electrocatalysts under PEM Fuel Cell Conditions. *Electrochim. Acta* **2010**, *55*, 9024−9034.

(41) Chan, M.-H.; Lu, F.-H. X-Ray Photoelectron Spectroscopy Analyses of Titanium Oxynitride Films Prepared by Magnetron Sputtering Using Air/Ar Mixtures. *Thin Solid Films* **2009**, *517*, 5006−5009.

(42) Chen, H.-Y.; Lu, F.-H. Oxidation Behavior of Titanium Nitride Films. *J. Vac. Sci. Technol., A* **2005**, *23*, 1006−1009.

(43) Mucha, N. R.*Development of Titanium Nitride Based Oxynitride Thin Film Systems for Alternative Energy Applications, North Carolina Agricultural and Technical State University*. 2020.

(44) Cao, Y. Q.; Zhao, X. R.; Chen, J.; Zhang, W.; Li, M.; Zhu, L.; Zhang, X. J.; Wu, D.; Li, A. D. TiO_xN_y Modified TiO_2 Powders Prepared by Plasma Enhanced Atomic Layer Deposition for Highly Visible Light Photocatalysis. *Sci. Rep.* **2018**, *8*, 12131.

(45) McKenna, K.; Structure, P. Electronic Properties, and Oxygen Incorporation/Diffusion Characteristics of the Σ 5 TiN (310)[001] Tilt Grain Boundary. *J. Appl. Phys.* **2018**, *123*, No. 075301.

(46) Jaeger, D.; Patscheider, J. A Complete and Self-Consistent Evaluation of XPS Spectra of TiN. *J. Electron Spectrosc. Relat. Phenom.* **2012**, *185*, 523−534.

(47) Biesinger, M. C.; Lau, L. W.; Gerson, A. R.; Smart, R. S. C. Resolving Surface Chemical States in XPS Analysis of First Row Transition Metals, Oxides and Hydroxides: Sc, Ti, V, Cu and Zn. *Appl. Surf. Sci.* **2010**, *257*, 887−898.

(48) Rasic, D.; Sachan, R.; Chisholm, M. F.; Prater, J.; Narayan, J. Room Temperature Growth of Epitaxial Titanium Nitride Films by Pulsed Laser Deposition. *Cryst. Growth Des.* **2017**, *17*, 6634−6640.

(49) Roy, M.; Mucha, N. R.; Ponnam, R. G.; Jaipan, P.; Scott-Emuakpor, O.; Yarmolenko, S.; Majumdar, A. K.; Kumar, D. Quantum Interference Effects in Titanium Nitride Films at Low Temperatures. *Thin Solid Films* **2019**, *681*, 1−5.

(50) Thompson, A. P.; Aktulga, H. M.; Berger, R.; Bolintineanu, D. S.; Brown, W. M.; Crozier, P. S.; in 't Veld, P. J.; Kohlmeyer, A.; Moore, S. G.; Nguyen, T. D.; Shan, R.; Stevens, M. J.; Tranchida, J.; Trott, C.; Plimpton, S. J. Lammps - a Flexible Simulation Tool for Particle-Based Materials Modeling at the Atomic, Meso, and Continuum Scales. *Comput. Phys. Commun.* **2022**, *271*, 108171.

(51) Stukowski, A. Visualization and Analysis of Atomistic Simulation Data with Ovito−the Open Visualization Tool. *Modell. Simul. Mater. Sci. Eng.* **2009**, *18*, No. 015012.

(52) Cheng, Y. T.; Liang, T.; Martinez, J. A.; Phillpot, S. R.; Sinnott, S. B. A Charge Optimized Many-Body Potential for Titanium Nitride (TiN). *J. Phys.: Condens. Matter* **2014**, *26*, 265004.

(53) Cheng, Y.-T.; Shan, T.-R.; Liang, T.; Behera, R. K.; Phillpot, S. R.; Sinnott, S. B. A Charge Optimized Many-Body (Comb) Potential for Titanium and Titania. *J. Phys.: Condens. Matter* **2014**, *26*, 315007.

(54) Liang, T.; Devine, B.; Phillpot, S. R.; Sinnott, S. B. Variable Charge Reactive Potential for Hydrocarbons to Simulate Organic-Copper Interactions. *J. Phys. Chem. A* **2012**, *116*, 7976−7991.

(55) Khwansungnoen, P.; Chaiyakun, S.; Rattana, T. Room Temperature Sputtered Titanium Oxynitride Thin Films: The Influence of Oxygen Addition. *Thin Solid Films* **2020**, *711*, 138269.

(56) Smith, W.; Fakhouri, H.; Pulpytel, J.; Arefi-Khonsari, F. Control of the Optical and Crystalline Properties of TiO_2 in Visible-Light Active TiO_2/TiN Bi-Layer Thin-Film Stacks. *J. Appl. Phys.* **2012**, *111*, No. 024301.

(57) Makuła, P.; Pacia, M.; Macyk, W. How to Correctly Determine the Band Gap Energy of Modified Semiconductor Photocatalysts Based on Uv−Vis Spectra. *J. Phys. Chem. Lett.* **2018**, *9*, 6814−6817.

(58) Xie, Z.; Liu, X.; Zhan, P.; Wang, W.; Zhang, Z. Tuning the Optical Bandgap of TiO_2-TiN Composite Films as Photocatalyst in the Visible Light. *AIP Adv.* **2013**, *3*, No. 062129.

(59) Smardz, L.; Köbler, U.; Zinn, W. Oxidation Kinetics of Thin and Ultrathin Cobalt Films. *J. Appl. Phys.* **1992**, *71*, 5199−5204.

(60) Marczyńska, A.; Skoryna, J.; Lewandowski, M.; Smardz, L. Oxidation Kinetics of Thin and Ultrathin Fe Films. *Acta Phys. Pol., A* **2015**, 127.

(61) Friesen, C.; Seel, S. C.; Thompson, C. V. Reversible Stress Changes at All Stages of Volmer−Weber Film Growth. *J. Appl. Phys.* **2004**, *95*, 1011−1020.

(62) Yu, H. Z.; Thompson, C. V. Grain Growth and Complex Stress Evolution During Volmer−Weber Growth of Polycrystalline Thin Films. *Acta Mater.* **2014**, *67*, 189−198.

(63) Rogers, B.; Adams, J.; Pennathur, S.*Nanotechnology: Understanding Small Systems*; Crc Press. 2014

(64) Roy, M.; Mucha, N. R.; Fialkova, S.; Kumar, D. Effect of Thickness on Metal-to-Semiconductor Transition in 2-Dimensional TiN Thin Films. *AIP Adv.* **2021**, *11*, No. 045204.

(65) Roy, M.; Kumar, D.Ultra-Low Thickness Titanium Nitride Thin Films for Spintronic Devices. *Bull. Am. Phys. Soc.***2022**.

(66) Nie, J.; Yang, J.; Piao, Y.; Li, H.; Sun, Y.; Xue, Q.; Xiong, C.; Dou, R.; Tu, Q. Quantum Confinement Effect in Zno Thin Films Grown by Pulsed Laser Deposition. *Appl. Phys. Lett.* **2008**, *93*, 173104.

(67) Nie, J. C.; Hua, Z. Y.; Dou, R. F.; Tu, Q. Y. Quantum Confinement Effect in High Quality Nanostructured CeO_2 Thin Films. *J. Appl. Phys.* **2008**, *103*, No. 054308.

(68) Anandh Jesuraj, S.; Devadason, S.; Melvin David Kumar, M. Effect of Quantum Confinement in Cdse/Se Multilayer Thin Films Prepared by Pvd Technique. *Mater. Sci. Semicond. Process.* **2017**, *64*, 109−114.

(69) Shah, D.; Catellani, A.; Reddy, H.; Kinsey, N.; Shalaev, V.; Boltasseva, A.; Calzolari, A. Controlling the Plasmonic Properties of Ultrathin TiN Films at the Atomic Level. *ACS Photonics* **2018**, *5*, 2816−2824.

(70) Haydous, F.; Dobeli, M.; Si, W.; Waag, F.; Li, F.; Pomjakushina, E.; Wokaun, A.; Gökce, B.; Pergolesi, D.; Lippert, T. Oxynitride Thin Films Versus Particle-Based Photoanodes: A Comparative Study for Photoelectrochemical Solar Water Splitting. *ACS Appl. Energy Mater.* **2019**, *2*, 754−763.

https://doi.org/10.1021/acsami.2c18926